

Intercalation makes the difference with TiS₂: Boosting electrocatalytic water oxidation activity through Co intercalation

Aron J. Huckaba^{a)}

Group for Molecular Engineering of Functional Materials, Institute of Chemical Sciences and Engineering, Ecole Polytechnique Fédérale de Lausanne Valais, Sion 1951, Switzerland

Maryline Ralairisoa

Humboldt Universität zu Berlin, Institut für Physik & Integrative Research Institute for the Sciences Adlershof, Berlin 12489, Germany

Kyung Taek Cho

Group for Molecular Engineering of Functional Materials, Institute of Chemical Sciences and Engineering, Ecole Polytechnique Fédérale de Lausanne Valais, Sion 1951, Switzerland

Emad Oveisi

Interdisciplinary Centre for Electron Microscopy, Ecole Polytechnique Fédérale de Lausanne, Lausanne 1015, Switzerland

Norbert Koch

Humboldt Universität zu Berlin, Institut für Physik & Integrative Research Institute for the Sciences Adlershof, Berlin 12489, Germany

Mohammad Khaja Nazeeruddin

Group for Molecular Engineering of Functional Materials, Institute of Chemical Sciences and Engineering, Ecole Polytechnique Fédérale de Lausanne Valais, Sion 1951, Switzerland

(Received 10 August 2017; accepted 17 October 2017)

Intercalated and unmodified TiS₂ nanomaterials were synthesized and characterized by UV-Visible-NIR spectroscopy, Powder X-Ray Diffraction, and X-Ray Photoelectron and Ultraviolet Photoelectron Spectroscopy. Photoelectron spectroscopy measurements indicated that CoS and Cu₂S appeared to be intercalated between sheets of partially or fully oxidized TiS₂, which could be solution processed on conductive oxide substrates. The materials were then applied toward water oxidation and evaluated by cyclic voltammetry, chronoamperometry, and impedance measurements. While unmodified TiS₂ was not observed to perform well as an electrocatalyst with overpotentials >3 V in 1 M NaOH electrolyte, CoS intercalation was found to lower the overpotential by ~1.8–1.44 V at 10 mA/cm². Conversely, Cu₂S intercalation resulted in only a modest increase in performance (>2.3 V overpotential). Impedance measurements indicated that intercalation increased the series resistance in the as-prepared samples but decreased the series resistance in oxidized samples.

I. INTRODUCTION

Efficient conversion of water to hydrogen and oxygen with solar energy will become increasingly important in the future.¹ The sun is the earth's only energy input and it supplies all of humanity's annual energy in a matter of hours. Therefore, whether the sunlight is directly utilized through photoelectrochemical methods or through solar-driven electrochemical methods, identifying materials capable of efficiently catalyzing the oxygen evolution reaction (OER) is an important challenge for the development of solar fuel generators.^{2,3} This four-electron, four-proton reaction producing a diatomic gas is one of the most

important on earth. Indeed, the electrons used to make fuels of all sorts should likely originate from the OER.^{4,5}

The thermodynamic potential of the four electron, four proton overall water splitting reaction, $2 \text{H}_2\text{O} (\text{l}) \rightarrow 2 \text{H}_2 (\text{g}) + \text{O}_2 (\text{g})$, is $E^0 = -1.23 \text{ V}$. At all pH values, larger overpotentials (potential above the thermodynamic potential required to overcome kinetic barriers) are required to drive this reaction one electron at a time than if moving four electrons and protons at the same time. The half reactions controlling each step are different depending on the solution pH. At pH = 14, the water oxidation half reaction ($4 \text{OH}^- \rightarrow \text{O}_2 (\text{g}) + 2 \text{H}_2\text{O} (\text{l}) + 4 \text{e}^-$) has $E^0 = -0.40 \text{ V}$, while at pH = 0, the water oxidation half reaction ($2 \text{H}_2\text{O} (\text{l}) \rightarrow \text{O}_2 (\text{g}) + 4 \text{H}^+ + 4 \text{e}^-$) has $E^0 = -1.23 \text{ V}$. Conversely, the water reduction half reaction has $E^0 = 0.00 \text{ V}$ at pH = 0 ($4 \text{H}^+ + 4 \text{e}^- \rightarrow 2 \text{H}_2 (\text{g})$) and $E^0 = -0.83 \text{ V}$ at pH = 14 ($4 \text{H}_2\text{O} (\text{l}) + 4 \text{e}^- \rightarrow 2 \text{H}_2 (\text{g}) +$

Contributing Editor: Artur Braun

^{a)}Address all correspondence to this author.

e-mail: aron.huckaba@epfl.ch

DOI: 10.1557/jmr.2017.431

4 OH⁻). In nature, water oxidation is affected by the calcium-manganese-oxo water oxidizing complex of photosystem II,⁶ which functions through the “Kok cycle,” in which one proton and one electron leave the reactive complex at a time.⁷

The seminal work by Fujishima and Honda in 1972 showed that TiO₂ could function as a water oxidation catalyst, albeit poorly.⁸ Since then, many other water oxidation catalysts have been reported in the literature based on both homogeneous^{9,10} and heterogeneous materials.³ These heterogeneous materials include metals,¹¹ alloys,¹² and crystalline metal oxides.^{13,14} State-of-the-art materials based on either metal/metal oxides such as IrO₂,^{15–17} RuO₂,¹⁷ or Pt,¹⁶ or nonprecious metal oxides such as Mn₂O₃,¹⁸ Co₃O₄,¹⁹ NiFeO_x,¹⁶ and NiCo²⁰ normally reach 450 mV when operated at pH 14, with fewer reaching <350 mV when operated in the same conditions.¹⁵ Many of these catalysts can be fabricated on glassy carbon substrates using electrochemical deposition at large negative potentials.¹⁶ Less frequently, high-performing state-of-the-art water oxidation catalysts purposefully based on nanoparticles have been reported. Particles based on materials such as CoMnP,²¹ CoFeP,²² Mn₅O₈,²³ and CoO²⁴ have exhibited high performance.

Research on TiS₂ began in earnest decades ago as a cathode material for lithium ion batteries thanks to rapid, reversible intercalation and good electrical conductivity.^{25–27} Studies on TiS₂ and other 2D-layered materials (chalcogenides and others including graphene) have increased rapidly in recent years, with thousands of manuscripts now being published each year, thanks to some remarkable properties like high mobility [200,00 cm²/(V s)], high optical transparency (97.7%), and high thermal conductivity [53,000 W/(m K)].^{28,29} Furthermore, many research groups have and are actively studying intercalation of the *s* block and transition metals into 2D chalcogenide materials, with intercalation often drastically changing physical properties of the original material.³⁰ Even though much effort was put into understanding the ramifications of TiS₂ intercalation,^{31–33} studies using this material have somewhat lessened in recent years.^{34–37}

Our approach to synthesizing new water oxidation catalysts stemmed directly from our previous work with transition metal sulfide materials for inclusion as hole transport materials (HTM) in perovskite solar cells. We recently synthesized amorphous TiS₂ nanoparticles that were highly conductive at low film thicknesses and found they functioned well as HTM materials even though they were heavily oxidized.³⁸ The particles were amorphous and could be intercalated with organic or inorganic species. Because the particles themselves retained their overall structure upon oxidation, we hypothesized that intercalating catalytically active metal atoms between the TiS₂ sheets would lead to stable water oxidation catalysts with improved reactivity over unmodified TiS₂. Herein,

we report for the first time the synthesis and characterization of amorphous, oxidized TiS₂ materials intercalated with Cu₂S or CoS, which resulted from the oxidation of intercalated amorphous TiS₂. Using these materials, we have realized a substantial enhancement in water oxidation in 1 M NaOH electrolyte solutions using Co intercalated TiS₂, from 3.0 V overpotential at 10 mA/cm to 1.44 V overpotential.

II. EXPERIMENTAL SECTION

A. General considerations

All chemicals were purchased and used without further purification. TiCl₄ was purchased from Sigma Aldrich (Quentin-Fallavier, France). Electrochemical measurements were measured with a Biologic S-200 cyclic voltammeter, and all measurements were performed in quiescent solutions. Cyclic voltammograms were measured with a standard three electrode configuration using a platinum foil counter electrode and a saturated Ag/AgCl reference electrode. The reference electrode was equipped with a porous Vycor tip and was measured to be 0.964 versus NHE in 1.0 M NaOH solution. UV-Vis spectra were measured with a Cary 5000 UV-Vis spectrometer (CARY, Le Locle, Switzerland). Powder X-Ray Diffraction (PXRD) data were measured with a Bruker Avance D8 (Bruker, Karlsruhe, Germany) irradiated at 1.54058 Å using a Cu source.

B. Synthesis of TiS₂ materials

For each of the materials (TiS₂ and intercalated versions), the following procedure was used, with either 1 equiv TiCl₄ (as below) or 0.5 equiv TiCl₄ and 0.5 equiv metal precursor (CuCl or CoCl₂). A flame-dried flask was charged with a stirbar and oleylamine (50 mL) under N₂. The solution was warmed to 140 °C with stirring and strong N₂ sparging. After 30 min of sparging at 140 °C, TiCl₄ (1 equiv, 0.5 mL, 4.5 mmol) was added via syringe, and sparging and stirring at 140 °C continued. The reaction generated HCl vigorously, and once the reaction was complete, a reddish solution was obtained. The solution at this stage can vary in color from orange to dark red depending on the concentration of TiCl₄. After 5 min, if necessary, the second metal precursor was added (0.5 equiv, 2.25 mmol). The mixture was allowed to be stirred at 120 °C. After 30 min, the temperature was increased to 225 °C with stirring. During this time, sulfur (99%, flowers, Alfa Aesar, Haverhill, Massachusetts, 4 equiv, 0.72 g, 22.5 mmol) was suspended in Oleylamine (15 mL) and then was sonicated for 15 min and warmed to 120 °C with stirring until all sulfur had dissolved. Once the temperature of both reaction mixtures was reached, the sulfur mixture was quickly injected into the metal precursor solution. The reaction mixture

temperature dropped to 190 °C, and the solution was allowed to be warmed to 225 °C with stirring. The solution immediately turned black. After 30 min, the reaction mixture was cooled to room temperature by submerging the flask in water. Once cooled, methanol (40 mL) was added, and the formed precipitate was isolated by centrifugation. The precipitate was then dissolved in toluene and precipitated with methanol, and this procedure was repeated more than twice to remove all the unreacted sulfur. The precipitate was then dissolved in 10 mL toluene and stored in the glovebox for further use.

C. Electrode preparation

Fluorine-doped tin oxide (FTO) coated glass-substrates (NSG10) were sequentially washed by Helmanex, water, and isopropanol in an ultrasonic bath for 40 min. A solution of TiS₂ materials was deposited by spincoating at 2000 rpm for 30 s in a glovebox, then a 20 μL aliquot of the same solution was dropcasted and the films were annealed for 5 min at 180 °C. The active area of the electrode was masked to 1 mA/cm² before film deposition.

D. UPS and XPS analysis

Ultraviolet photoelectron spectroscopy (UPS) measurements were performed in an ultra-high vacuum analysis chamber (base pressure <10⁻⁹ mbar) using a He-discharge UV source (Omicron, Taunusstein, Germany) with an excitation energy of 21.2 eV. The UPS spectra were recorded using a Phoibos 150 (Specs, Berlin, Germany) hemispherical energy analyzer. For the work function determination, the secondary electron cutoff (SECO) was recorded by applying a -10 V sample bias to clear the analyzer work function. The reported valence band spectra were background subtracted. The X-ray photoemission spectroscopy (XPS) measurements were performed with a JPS-9030 hemispherical photoelectron spectrometer (Jeol, Freising, Germany) instrument using a monochromatic Al K_α X-ray source. The overall resolution was 1.25 and 0.68 eV for CoTiS₂ and CuTiS₂, respectively (as determined from the full-width half-maximum of the Ag 3d_{5/2} core level at a pass energy of 30 and 10 eV, respectively). The binding energies for all the photoemission spectra are referenced to the Fermi level. The base pressure in the analysis chamber for the XPS analysis was 2 × 10⁻¹⁰ mbar. A mixed Gaussian/Lorentzian peak shape and a Shirley-type background were used for the XPS peak fitting with the XPS Peak 4.1 software (Raymond Kwok).

III. RESULTS AND DISCUSSION

A. Materials synthesis and characterization

The TiS₂ materials were synthesized in a simple two step hydrothermal method similar to our previous work.³⁸

Briefly, after solvating the metal precursor (either TiCl₄ or TiCl₄ and CuCl or CoCl₂ in equimolar quantities) in dried, degassed oleylamine, the temperature was elevated and sulfur was added. After 30 min of particle growth, the solution was cooled and the dark precipitate was collected by centrifugation. While much effort was undertaken to ensure that TiS₂ did not oxidize during particle synthesis, there were several manipulations/steps after the synthesis where particle oxidation could occur, such as precipitation by addition of MeOH, isolation of particles in ambient atmosphere, and annealing in a glovebox with some water (<1 ppm) and oxygen (<30 ppm) present. The materials made in this manner were: TiS₂, Co_{0.5}Ti_{0.5}S₂ (hereafter called CoTiS₂), and Cu_{0.5}Ti_{0.5}S₂ (hereafter called CuTiS₂).^{39,40} Once synthesized, the materials were stored in a glovebox to minimize further particle oxidation. Particle suspensions were spin coated onto substrates before annealing at 180 °C in the glovebox, hereafter termed “as-prepared” films, or annealed at 180 °C in the glovebox followed by annealing at 250 °C in ambient air, hereafter termed “oxidized” (Fig. 1). Nevertheless, because we were interested in obtaining the overall structure of the intercalated TiS₂ particles, that is thin sheets with variable interlayer distances and thicknesses, and we had previously observed that this morphology does not change with oxidation, we were not concerned about excluding oxygen during every manipulation.

Once synthesized, each of the materials was studied by PXRD to understand the structural ramifications of Cu or Co inclusion. Each of the materials was deposited on a glass slide and found to be amorphous, with no significant crystalline phases apparent (Fig. 2), as has been observed by us and others.^{38,41,42} The diffraction signal between 7 and 10° in the as-prepared TiS₂ was assigned as an interlayer gap *c* axis peak (001) due to the intercalated organic oleylamine ligand.⁴³ Broad signals were also observed near 30° and 45°, which are present in a variety of amorphous TiS₂ or TiO₂ materials reported in the literature.^{44,45} In the bulk powder samples of the as-prepared and oxidized TiS₂, a signal near 55°, to the (110) peak, was evident;³⁹ however, films deposited from well-dispersed solutions did not have this same peak. This indicated that the majority of particles in the film were not face-on aggregates. These two intense, clear diffraction signals in addition to the broad nature of the other peaks indicate that each of the nanomaterials was morphologically characterized as very small (<50 nm) sized thin sheets with variable interlayer distances, which has been observed by others in similar systems.^{43,46} For the CuTiS₂ material, the same amorphous signals near 30° and 45° were observed, but two additional peaks were also present, near 50° and 30° that was assigned to Cu₂S.⁴⁷ A similar observation was made for the CoTiS₂ material, with signals corresponding to CoS observed

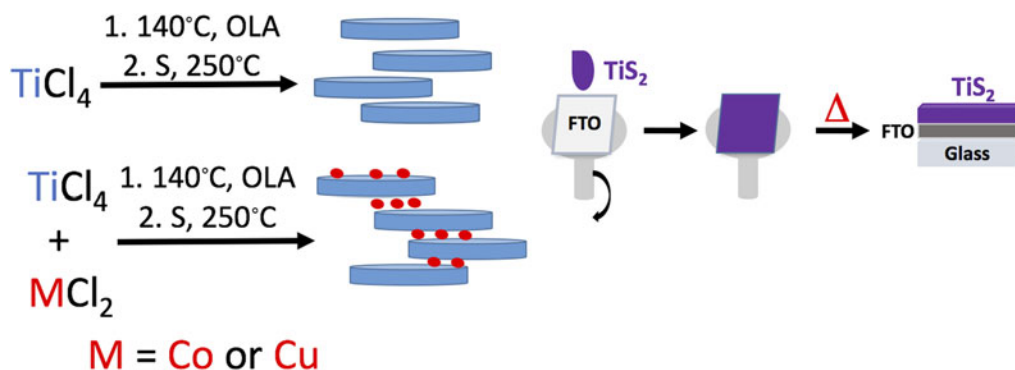


FIG. 1. Left: The synthetic scheme for TiS₂ materials. Right: The film deposition process.

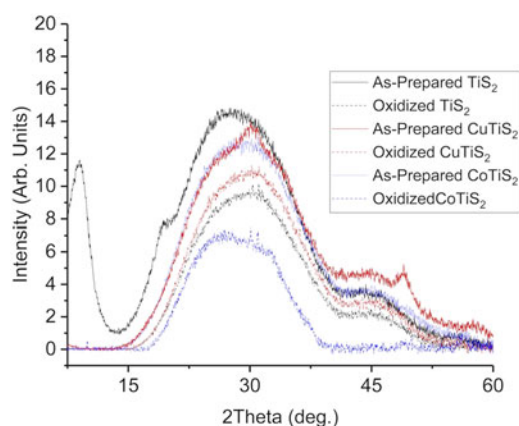


FIG. 2. PXRD data of TiS₂, CuTiS₂, and CoTiS₂ thin films deposited on glass. “As-prepared” indicates annealing in an N₂-filled glovebox at 180 °C, and “oxidized” indicates annealing in an N₂-filled glovebox at 180 °C followed by annealing at 250 °C in ambient conditions.

near 30°, 48°, and 58°.⁴⁸ Films of each material were then measured after annealing at 250 °C in ambient conditions to understand how oxidation affected the material. In each material, only the broad signals near 30° and 45° remained.

Scanning electron microscopy (SEM) investigations were undertaken next to better understand the material film morphology. Previous investigations on TiS₂ nano-materials by us revealed that powder samples and suspensions stored in air display a wide particle size distribution and poor solubility in organic solvents.³⁸ This wide particle size distribution (<10 nm to <200 nm) led to large differences in film quality and morphology depending on spin-coating speed. Conversely, the as-prepared TiS₂ materials in this work stored in the glovebox are highly soluble in organic solvents and easily processed by normal deposition methods to give smooth, uniform films, and the particle size was determined by the spin-coating deposition of low-concentration suspensions and SEM analysis (Fig. 3). Very small (~10 nm) and somewhat larger (10–50 nm) particles were present in the CoTiS₂ and

CuTiS₂ material (Fig. 3), while the TiS₂ particles exhibit narrow size distribution (Fig. 3). Spin coating at 2000 rpm for 30 s yielded a 200 nm thick layer of CoTiS₂ (See Supplementary Material). Dropcasting the nanoparticulate suspension onto a previously spin-coated film confirmed all suspended particles to be <50 nm.

Next, optoelectronic properties of the thin films were investigated to understand how the incorporation of Cu or Co influenced the material band gap (Fig. 4). In the unmodified TiS₂ material, two direct transitions at 580 and 363 nm and an indirect absorption onset at 850 nm were observed. The peak at 580 nm was not apparent in CoTiS₂ and diminished in CuTiS₂, which indicated the absence of TiS₂ in CoTiS₂ and a small quantity in CuTiS₂. In CuTiS₂, a transition at 350 nm with shoulders at 468, 507, and 582 nm, and an absorption onset of 660 nm were observed. For CoTiS₂, two shoulders at 485 and 533 nm are evident, with an absorption onset of 870 nm. The single absorption band present with TiS₂ indicated one major particle size present, while the multiple transitions indicated multiple size regimes, as has been reported before and was observed in SEM measurements.^{38,49}

B. Photoelectron spectroscopy

The SECO and valence band spectra recorded for CuTiS₂ and CoTiS₂ are shown in Fig. 5. The SECO of CuTiS₂ yields a work function of 4.10 eV [Fig. 5(a)], which is close to that of TiS₂, as previously measured (Supplementary Material, Fig. S2).³⁸ In comparison, the work function of CoTiS₂ is 0.4 eV lower than that of CuTiS₂. This might be due to the complete oxidation of Ti (into TiO₂) for CoTiS₂, as opposed to the only partially oxidized Ti in CuTiS₂. This interpretation is further supported by the XPS data presented in the following (vide infra). Most interestingly, in contrast to the TiS₂ sample (Supplementary Material, Fig. S2), the valence band spectra for both CuTiS₂ and CoTiS₂ show a detectable intensity up to the Fermi level (0–2 eV), which indicates the presence of a finite density of states in this binding energy region [Fig. 5(b)]. The presence

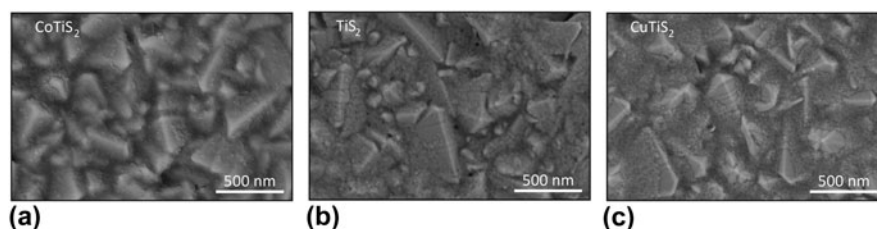


FIG. 3. Top-view SEM images of TiS₂ materials. (a) Top-view image of spin-coated low-concentration CoTiS₂ after annealing in an N₂-filled glovebox at 180 °C. (b) Top-view image of spin-coated low-concentration TiS₂ after annealing in an N₂-filled glovebox at 180 °C. (c) Top-view image of spin-coated low-concentration CuTiS₂ after annealing in an N₂-filled glovebox at 180 °C.

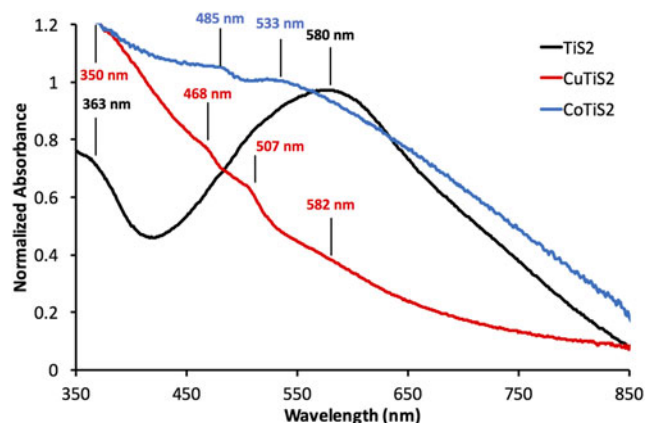


FIG. 4. Normalized UV-Vis absorption spectra of TiS₂, CuTiS₂, and CoTiS₂ thin films deposited on glass.

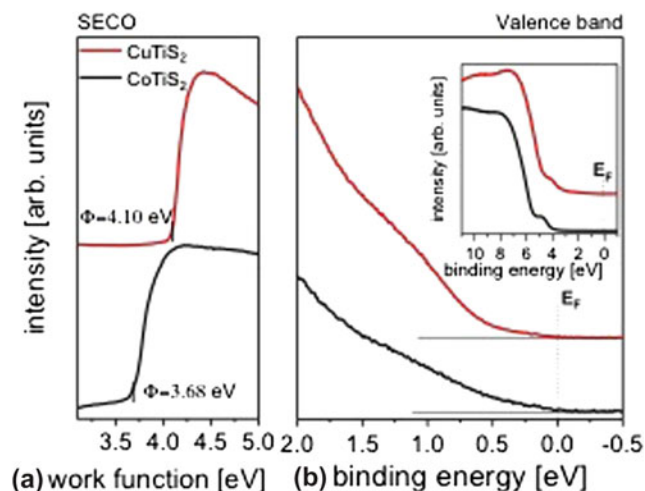


FIG. 5. (a) SECO and (b) the valence band spectra of CuTiS₂ (red) and CoTiS₂ (black) at low binding energies close to the Fermi level. The inset in (b) shows the large-range UPS spectra of both samples.

of such filled states, in contrast to the not-alloyed TiS₂ sample, likely suggests an electron transfer between Cu- and Co-related compounds and TiS₂. Furthermore, since the valence band spectra [Fig. 5(b), inset] of both samples show similar features to those of TiS₂ (Supplementary Material, Fig. S2), thus indicating that the TiS₂ valence band features are still the dominant ones, our results might indicate

a possible intercalation of Cu and Co or of Cu- and Co-related compounds within the TiS₂ and oxidized TiS₂ material, respectively.

XPS measurements were done to get information about the possible composition of the samples (Fig. 6). The XPS core level spectra of Ti 2*p*, S 2*p*, Cu 2*p*_{3/2}, and Co 2*p*_{3/2} for CuTiS₂ and CoTiS₂ are shown in Fig. 6. The binding energy values were all adjusted to the adventitious C 1*s* carbon binding energy that was here referenced to 285 eV (Supplementary Material, Fig. S3). For the Ti 2*p* and S 2*p* doublet peaks, the fitted peaks for each doublet are in the same color.

In Fig. 6(a), Ti 2*p* in CuTiS₂ exhibits three contributions with the highest contribution at 459 eV and 464.7 eV for Ti 2*p*_{3/2} and Ti 2*p*_{1/2}, respectively. This could be assigned to Ti 2*p* as in TiO₂,⁵⁰ thus implying that Ti is partially oxidized within the sample. Furthermore, the Ti 2*p*_{3/2} at 457.1 eV and S 2*p*_{3/2} at 161.5 eV [Fig. 6(b)] are at binding energy positions which are similar to those in TiS₂ (457 eV for Ti 2*p*_{3/2} and 161.3 eV for S 2*p*_{3/2}) in our previous work,³⁸ it is therefore possible that TiS₂ is still existing in CuTiS₂. The Ti 2*p*_{3/2} peak contribution at 455.3 eV corresponds to a lower oxidation state of Ti than in TiS₂ or TiO₂ that might represent TiO.⁵¹ The presence of Cu₂S is not excluded either as the S 2*p* and Cu 2*p* binding energies in Cu₂S would also be expected near the positions of the main peaks at 161.5 and 932.5 eV for S 2*p*_{3/2} and Cu 2*p*_{1/2}, respectively.⁵²

In contrast to the CuTiS₂ sample, the titanium in CoTiS₂ exhibits only one Ti 2*p* peak at 458.8 and 464.5 eV for Ti 2*p*_{3/2} and Ti 2*p*_{1/2}, respectively [Fig. 6(d)]. The high binding energy of Ti 2*p* indicates the presence of Ti as in TiO₂, thus showing that the TiS₂ in CoTiS₂ is fully oxidized into TiO₂. The sulfur main peak at 161.2 eV for S 2*p*_{3/2} and the cobalt Co 2*p*_{3/2} at 778.1 eV might be compared to S 2*p*_{3/2} and Co 2*p*_{3/2} as in CoS.^{53,54} One peak at 780.4 eV is also observed for Co 2*p*_{3/2}, which might represent a higher oxidation state of cobalt. However, this might correspond to a satellite line that has been observed before in CoS.⁵⁴ A sulfur S 2*p*_{3/2} peak is also detected at 163 and 162.8 eV for CuTiS₂ and CoTiS₂, respectively. These two peaks correspond to the previously reported undefined species⁵⁵ and that was also observed in TiS₂ and has been observed in other CoS_{*x*}

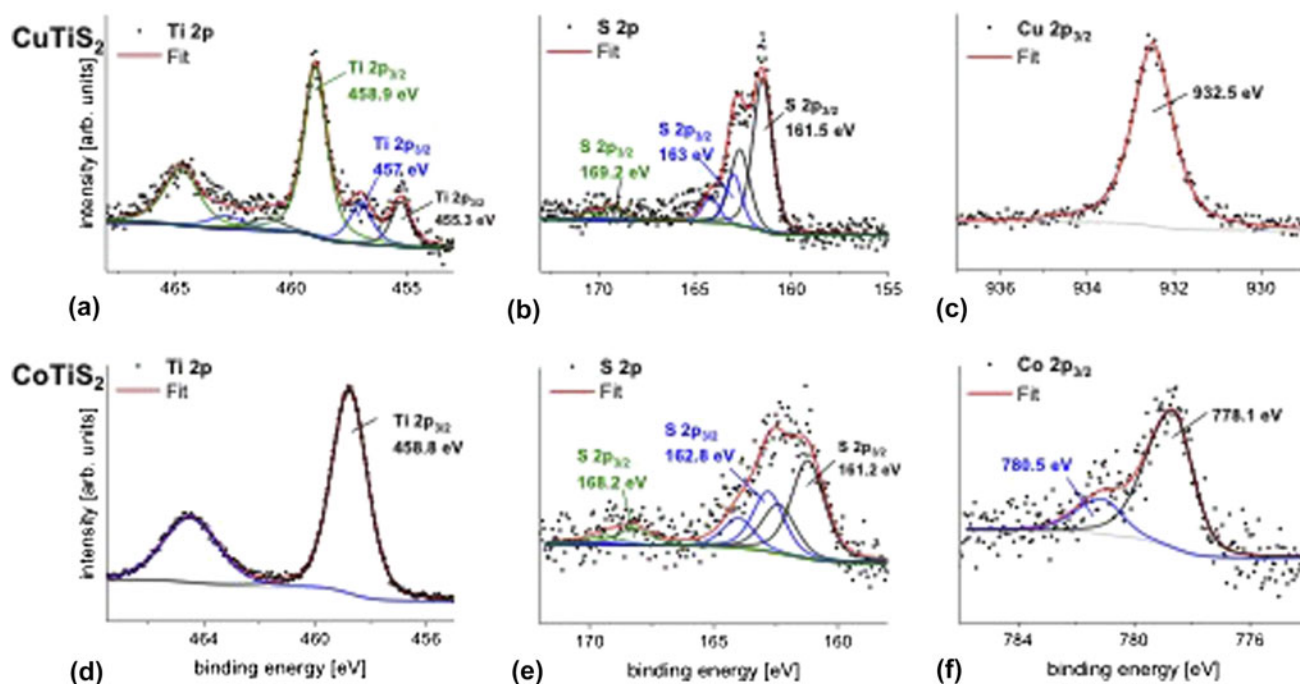


FIG. 6. XPS core level spectra of Ti 2p, S 2p, and Cu 2p_{3/2} in CuTiS₂ (a, b, and c, respectively) and Ti 2p, S 2p, and Co 2p_{3/2} in CoTiS₂ (d, e, and f, respectively). Data interpretation is in the text.

materials.^{38,56} Due to the short inelastic mean free path of electrons in solids, the photoelectrons detected by XPS are those located within a few nanometers beneath the surface. The XPS data have been recorded at a near normal emission (at 10° angle with respect to the surface normal) and yield a composition information depth of approximately 5 nm.

C. Electrochemical measurements and electrocatalysis

To evaluate the materials' activity in water oxidation electrocatalysis, a standard three electrode cyclic voltammetry setup was used, with a platinum foil counter electrode, a saturated Ag/AgCl reference electrode equipped with a porous vycor tip, and 1 M NaOH electrolyte. Working electrodes were annealed at 180 °C for five minutes in a glovebox to increase interparticle connectivity and substrate/film connectivity without oxygen, as TiS₂ materials are easily oxidized in ambient conditions and are partially oxidized by the trace of oxygen present in the glovebox during annealing.³⁸ This annealing step was important, as films deposited without annealing were mechanically unstable during measurement. An oxidative sweep of the purple TiS₂ film yielded an onset of current at ~1.53 V versus the normal hydrogen electrode (NHE) at 1 mA/cm. The passed current increased quickly with the increasing potential; however, no bubble formation was evident, and the observed current was unstable and noisy (See Supplementary Material). The film visibly changed from purple to pale yellow, which signaled the

oxidation of TiS₂. After this initial scan, the previously observed peak was not observed again and the onset of current underwent an anodic shift to >3.1 V versus NHE at 1 mA/cm (Fig. 7). Scans of the oxidized TiS₂ films are hereafter termed “oxidized” for clarity and consistency with the other materials studied here.

Obtaining the same cyclic voltammetry measurements with the intercalated TiS₂ materials yielded entirely different results. First scans of the glovebox annealed thin films yielded no discernible peaks until the appearance of a high potential activity onset (>2.6 V versus NHE at 1 mA/cm for CoTiS₂ and >2.75 V versus NHE at 1 mA/cm for CuTiS₂). Contrary to the nonmodified TiS₂ material, successive cycling of CV measurements produced more pronounced cathodic shifts of the onset of current for CoTiS₂, which shifted to 1.67 V versus NHE at 1 mA/cm after 50 cycles of cyclic voltammetry (data from similar films hereafter termed “partially oxidized”), see Supplementary Material. Two quasi-reversible waves were observed for CoTiS₂ at 1.12 and 1.27 V versus NHE and one reversible wave at 1.38 V versus NHE. The first quasi-reversible wave was assigned to the Co(II)/Co(III) redox couple, while the reversible wave was assigned to the Co(III)/Co(IV) redox couple.⁵⁷ These two oxidations likely represented the requisite complete oxidation of the intercalated CoS, and also indicated that the intercalated Co was in the +2 oxidation state. Observation of these phenomena also made clear that while the as-prepared or un-oxidized CoTiS₂ material did not exhibit high activity for water oxidation, the successively

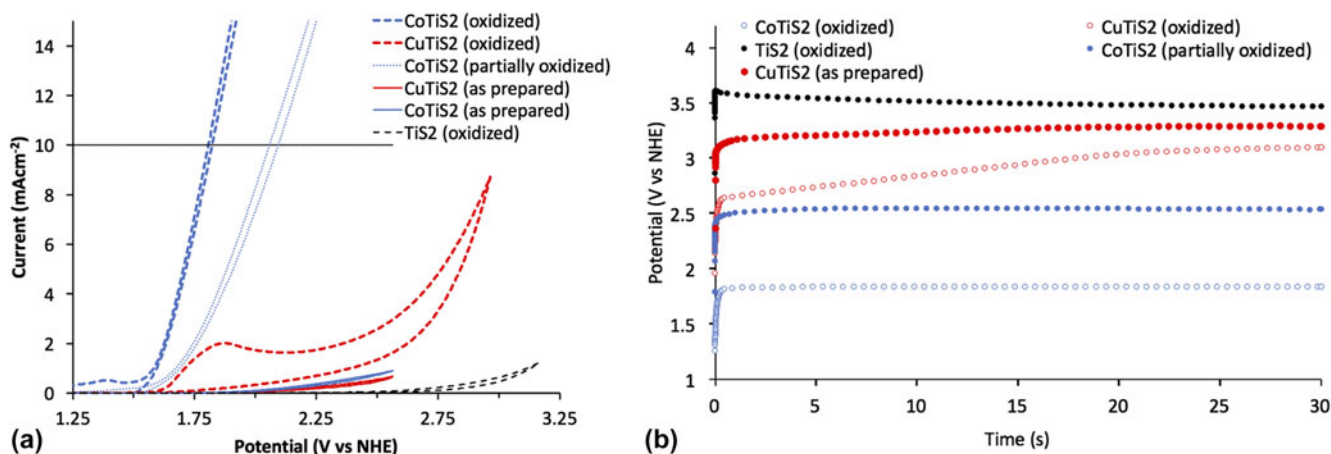


FIG. 7. (a) Cyclic voltammetric measurements and (b) chronoamperometric measurements of the as-prepared and oxidized samples of TiS₂, CuTiS₂, and CoTiS₂ in 1 M NaOH at 100 mV/s with the Pt foil counter electrode and the saturated Ag/AgCl reference electrode.

oxidized material led to a much higher activity likely through the formation of catalytically active CoO_x species [Fig. 7(a)]. Tangentially, observation of these oxidation waves also indicated that our reference electrode was indeed referenced correctly to be approximately 0.964 V versus NHE.

After this observation, films of each material were annealed in ambient air at 250 °C after the first annealing to maximize film oxidation. Whereas the as-prepared TiS₂ film maintained a dark color after annealing in the glovebox, samples annealed in ambient conditions lost their color. Intercalated materials retained their color after this annealing step, so to increase oxidation even further, an aliquot of the nanomaterial suspension was stored outside the glovebox for one week and then deposited on clean FTO substrates followed by annealing in ambient conditions at 250 °C. These films were observed to have largely lost all color, which indicated a widening of the optical band gap commensurate with the oxidative decomposition of TiS₂ to TiO₂. Oxidative sweeps of the CuTiS₂ films revealed an irreversible wave at 1.2 V versus NHE before onset of the activity, while the previously observed oxidative peaks for CoTiS₂ were enhanced. Based on the PES results, which indicated the presence of Cu₂S and TiS₂, this oxidative peak might represent the oxidation of the CuTiS₂ material to CuO_x and TiO₂ since it is similar to the onset of material oxidation in the as-prepared TiS₂ (Supplementary Material, Fig. S5). Bubble formation was observed for both films upon reaching the catalytic current, with increasing the rate of bubble formation and release with increasing potential.

Chronoamperometric measurements of each of the as-prepared films at 10 mA/cm over 30 s were then undertaken to better understand how sustained current affected the observed potential. The highest potential was observed for TiS₂ (3.47 V versus NHE, 3.07 V overpotential), followed by CuTiS₂ (3.29 V versus NHE,

2.89 V overpotential), and the highest performing was CoTiS₂ (2.54 V versus NHE, 2.14 V overpotential), with an observed potential almost 1 V lower than the unmodified TiS₂ [Figs. 7(b) and S6]. While the observed potential was observed to be static for the as-prepared samples for over 30 s, the observed potential dropped substantially to 2.11 V versus NHE (overpotential = 1.71 V) over 30 min (Supplementary Material, Fig. S7). Using the fully oxidized CuTiS₂ initially resulted in a lower observed potential (2.65 V versus NHE, 2.25 V overpotential) that quickly increased to near levels of the as-prepared film (3.1 V versus NHE, 2.70 V overpotential). Conversely, the oxidized CoTiS₂ film exhibited a highly stable potential of 1.84 V versus NHE (1.44 V overpotential) at 10 mA/cm, a drastic improvement of over 1.7 V from the unmodified TiS₂. This potential was stable for experiments with a long time period, and no change in the observed potential was observed after a continuous current measurement for 30 min, which indicated that the oxidized TiS₂ material was stable over this timeframe. Using this chronoamperometric data, a Tafel plot was constructed to estimate the Tafel slope of the catalysis, which indicates the potential difference between a decade of current (Supplementary Material, Fig. S9). For CoTiS₂, the Tafel slope was found to be 281 mV/decade.

Electrical Impedance Spectroscopy measurements were then undertaken to better understand the resistances present in each of the films. We measured the frequency-dependent complex impedance in a static solution under O₂ using the constructed working electrodes.¹⁶ Measuring between 100 Hz and 100 KHz in a nonFaradaic region allowed us to extract the real and imaginary components of the complex impedance and plot them for each of the films (Fig. 8). The data was then analyzed by standard BioLogic software using a standard Randles circuit to extract the series resistance (R_s), the charge-transfer resistance (R_{ct}),

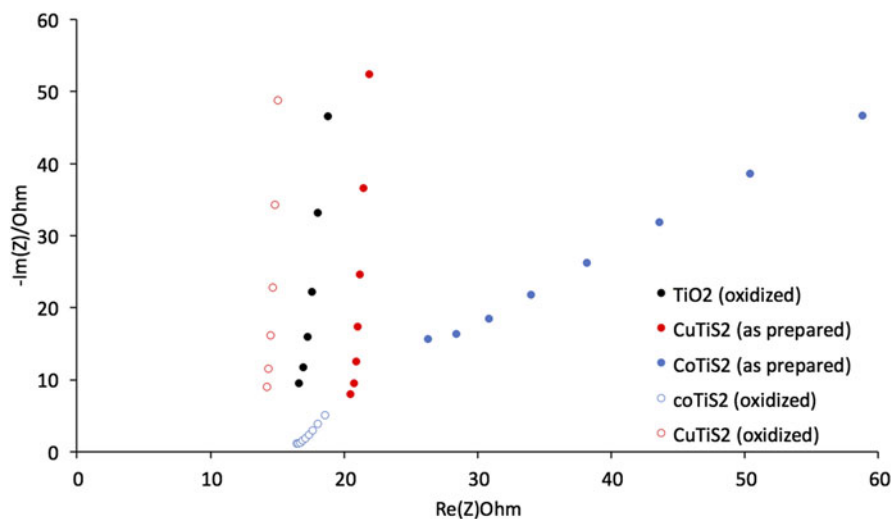


FIG. 8. The Nyquist plot of each of the materials described in 1 M NaOH.

Material	R_s (Ω)	R_{ct} (Ω)	C_{dl} (μF)
Oxidized TiS ₂	15.5	47.0×10^{-6}	2.17
As-prepared CuTiS ₂	19.4	58.2×10^{-6}	2.89
Oxidized CuTiS ₂	13.4	23.6×10^{-6}	23.6
As-prepared CoTiS ₂	17.7	177.	0.004
Oxidized CoTiS ₂	14.8	30.3×10^{-6}	0.040

and the double layer capacitance (C_{dl}) values. Broadly, the oxidized TiS₂ and both CuTiS₂ materials exhibit similar spectra, with large initial slopes of the respective semi-circles. The spectra for the CoTiS₂ materials, however, appear markedly different due to the presence of a 45° Warburg-type impedance signal for both.

Comparing the samples of each film in Fig. 8 indicates that as-prepared films intercalated with Cu or Co exhibit R_s higher than oxidized TiS₂ ($R_s = 15.5 \Omega$ for oxidized TiS₂, 19.4 Ω for the as-prepared CuTiS₂, and 17.7 Ω for the as-prepared CoTiS₂); however, upon oxidation, R_s is lower or similar for all three oxidized films ($R_s = 13.4 \Omega$ for oxidized CuTiS₂ and 14.8 Ω for oxidized CoTiS₂). Each of the intercalated materials exhibited higher R_{ct} values than the oxidized TiS₂, ($R_{ct} = 47.0 \mu\Omega$ for oxidized TiS₂, 58.2 $\mu\Omega$ for the as-prepared CuTiS₂, 23.6 $\mu\Omega$ for oxidized CuTiS₂, 177. Ω for the as-prepared CoTiS₂, and 30.3 $\mu\Omega$ for oxidized CoTiS₂), with the as-prepared CoTiS₂ exhibiting a much higher R_{ct} than the other materials. The C_{dl} values for the TiS₂ materials were found to also vary depending on intercalation and degree of oxidation. The as-prepared CuTiS₂ exhibited higher C_{dl} than the oxidized material, while the trend was opposite for CoTiS₂ ($C_{dl} = 2.17 \mu\text{F}$ for oxidized TiS₂, 2.89 μF for the as-prepared CuTiS₂, 23.6 μF for oxidized CuTiS₂, 0.004 μF for the as-prepared CoTiS₂, and 0.040 μF for oxidized CoTiS₂).

IV. CONCLUSIONS

Discovering efficient catalysts for the water oxidation half reaction is important, as this half reaction should theoretically supply the electrons for fuel forming reduction half reactions, such as those forming hydrogen (from water) and methanol (from CO₂). We have synthesized, characterized, and applied intercalated TiS₂ materials as water oxidation catalysts in 1 M NaOH electrolyte. Through intercalating precatalyst CoS between the sheets of TiS₂, the water oxidation overpotential was reduced by over 1.7 V at 10 mA/cm² compared to the unmodified TiS₂ material. CV studies indicated that the Co (II) species undergoes two successive oxidations before the catalytic signal is observed, implicating a catalytically active Co(IV) oxide active site. These cyclic voltammetry and chronoamperometric data match up well with other reported water oxidation catalysts, according to a recent report on catalyst benchmarking.¹⁶ At a current density of 10 mA/cm, the overpotential value of 1.44 V is much higher than the vast majority of state-of-the-art water oxidation catalysts. Nevertheless, the improvement of activity from unmodified TiO₂ is remarkable and indicates that intercalation/inclusion of catalyst materials into larger structures should serve as a way to boost performance. Future studies will focus on providing a better understanding of intercalating amorphous materials, in addition to optimizing the performance of intercalated materials, especially in regard to long-term stability.

ACKNOWLEDGMENTS

The authors acknowledge SNSF NRP 70 project; No. 407040 154056, European Commission H2020-ICT-2014-1, SOLEDLIGHT project, grant agreement No. 643791 and the Swiss State Secretariat for Education, Research, and Innovation (SERI), and CTI 15864.2 PFMN-NM, the

HZB-HU Graduate School “hybrid4energy,” and Solar-onix, Aubonne, Switzerland. A.H. acknowledges support from the special funding for energy research, managed by Prof. Andreas ZÜTTEL, Funds No. 563074.

REFERENCES

- M.G. Walter, E.L. Warren, J.R. McKone, S.W. Boettcher, Q. Mi, E.A. Santori, and N.S. Lewis: Solar water splitting cells. *Chem. Rev.* **110**, 6446 (2010).
- R. Eisenberg and H.B. Gray: Preface on making oxygen. *Inorg. Chem.* **47**, 1697 (2008).
- B.M. Hunter, H.B. Gray, and A.M. Mu: Earth-Abundant Heterogeneous Water Oxidation Catalysts. *Chem. Rev.* **116**, 14120 (2016).
- V. Artero and M. Fontecave: Solar fuels generation and molecular systems: Is it homogeneous or heterogeneous catalysis? *Chem. Soc. Rev.* **42**, 2338 (2013).
- T. Rosser and E. Reisner: Understanding immobilized molecular catalysts for fuel-forming reactions through UV/vis spectroelectrochemistry. *ACS Catal.* **7**, 3131 (2017).
- Y. Umena, K. Kawakami, J.-R. Shen, and N. Kamiya: Crystal structure of oxygen-evolving photosystem II at a resolution of 1.9 Å. *Nature* **473**, 55 (2011).
- B. Kok, B. Forbush, and M. McGloin: Cooperation of charges in photosynthetic O₂ evolution—I. A linear four step mechanism. *Photochem. Photobiol.* **11**, 457 (1970).
- A. Fujishima and K. Honda: Electrochemical photolysis of water at a semiconductor electrode. *Nature* **238**, 37 (1972).
- J.D. Blakemore, R.H. Crabtree, and G.W. Brudvig: Molecular catalysts for water oxidation. *Chem. Rev.* **115**, 12974 (2015).
- M. Yagi and M. Kaneko: Molecular catalysts for water oxidation. *Chem. Rev.* **101**, 21 (2001).
- J.P. Hoare: *The Electrochemistry of Oxygen* (John Wiley and Sons, Inc., New York, 1968).
- K. Lian, S.J. Thorpe, and D.W. Kirk: The electrocatalytic activity of amorphous and crystalline Ni–Co alloys on the oxygen evolution reaction. *Electrochim. Acta* **37**, 169 (1992).
- J. Suntivich, K.J. May, H.A. Gasteiger, J.B. Goodenough, and Y. Shao-Horn: A perovskite oxide optimized for oxygen evolution catalysis from molecular orbital principles. *Science* **334**, 1383 (2011).
- J.O. Bockris and T. Otagawa: Mechanism of oxygen evolution on perovskites. *J. Phys. Chem.* **87**, 2960 (1983).
- M. Driess, P.W. Menezes, A. Indra, V. Gutkin, and M. Driess: Boosting electrochemical water oxidation through replacement of O_h Co sites in cobalt oxide spinel with manganese. *Chem. Commun.* **53**, 8018 (2017).
- C.C.L. McCrory, S. Jung, J.C. Peters, and T.F. Jaramillo: Benchmarking heterogeneous electrocatalysts for the oxygen evolution reaction. *J. Am. Chem. Soc.* **135**, 16977 (2013).
- S. Trasatti: Electrocatalysis by oxides—Attempt at a unifying approach. *J. Electroanal. Chem. Interfacial Electrochem.* **111**, 125 (1980).
- Z.N. Zahran, E.A. Mohamed, T. Ohta, and Y. Naruta: Electrocatalytic water oxidation by a highly active and robust α-Mn₂O₃ thin film sintered on a fluorine-doped tin oxide electrode. *ChemCatChem* **8**, 532 (2016).
- J.D. Blakemore, H.B. Gray, J.R. Winkler, and A.M. Mu: Co₃O₄ nanoparticle water-oxidation catalysts made by pulsed-laser ablation in liquids. *ACS Catal.* **3**, 2497, (2013).
- H. Liang, F. Meng, M. Cabán-Acevedo, L. Li, A. Forticaux, L. Xiu, Z. Wang, and S. Jin: Hydrothermal continuous flow synthesis and exfoliation of NiCo layered double hydroxide nanosheets for enhanced oxygen evolution catalysis. *Nano Lett.* **15**, 1421 (2015).
- D. Li, H. Baydoun, N. Verani, and S.L. Brock: Efficient water oxidation using CoMnP nanoparticles. *J. Am. Chem. Soc.* **138**, 4006 (2016).
- A. Mendoza-Garcia, H. Zhu, Y. Yu, Q. Li, L. Zhou, D. Su, M.J. Kramer, and S. Sun: Controlled anisotropic growth of Co–Fe–P from Co–Fe–O nanoparticles. *Angew. Chem., Int. Ed.* **54**, 9642 (2015).
- D. Jeong, K. Jin, S.E. Jerng, H. Seo, D. Kim, S.H. Nahm, S.H. Kim, and K.T. Nam: Mn₅O₈ nanoparticles as efficient water oxidation catalysts at neutral pH. *ACS Catal.* **5**, 4624 (2015).
- L. Liao, Q. Zhang, Z. Su, Z. Zhao, Y. Wang, Y. Li, X. Lu, D. Wei, G. Feng, Q. Yu, X. Cai, J. Zhao, Z. Ren, H. Fang, F. Robles-Hernandez, S. Baldelli, and J. Bao: Efficient solar water-splitting using a nanocrystalline CoO photocatalyst. *Nat. Nanotechnol.* **9**, 69 (2014).
- M.S. Whittingham: Electrical energy storage and intercalation chemistry. *Science* **192**, 1126 (1976).
- M.S. Whittingham: Lithium batteries and cathode materials. *Chem. Rev.* **104**, 4271 (2004).
- L.E. Conroy and K.C. Park: Electrical properties of the group IV disulfides, titanium disulfide, zirconium disulfide, hafnium disulfide and tin disulfide. *Inorg. Chem.* **7**, 459 (1968).
- W. Choi, N. Choudhary, G.H. Han, J. Park, D. Akinwande, and Y.H. Lee: Recent development of two-dimensional transition metal dichalcogenides and their applications. *Mater. Today* **20**, 116 (2017).
- F. Bonaccorso, Z. Sun, T. Hasan, and A.C. Ferrari: Graphene photonics and optoelectronics. *Nat. Photonics* **4**, 611 (2010).
- Y. Jung, Y. Zhou, and J.J. Cha: Intercalation in two-dimensional transition metal chalcogenides. *Inorg. Chem. Front.* **3**, 452 (2016).
- M.H. Lindic, B. Pecquenard, P. Vinatier, A. Levasseur, H. Martinez, D. Gonbeau, P.E. Petit, and G. Ouvrard: Electrochemical mechanisms during lithium insertion into TiO_{0.6}S_{2.8} thin film positive electrode in lithium microbatteries. *J. Electrochem. Soc.* **152**, A141 (2005).
- G. Scholz, P. Joensen, J.M. Reyes, and R.F. Frindt: Intercalation of Ag in TaS₂ and TiS₂. *Physica B+C* **105**, 214 (1981).
- G.A. Wiegers: Misfit layer compounds: Structures and physical properties. *Prog. Solid State Chem.* **24**, 1 (1996).
- B. Tian, W. Tang, K. Leng, Z. Chen, S.J.R. Tan, C. Peng, G-H. Ning, W. Fu, C. Su, G.W. Zheng, and K.P. Loh: Phase transformations in TiS₂ during K intercalation. *ACS Energy Lett.* **2**, 1835 (2017).
- E. Guilmeau, A. Maignan, C. Wan, and K. Koumoto: On the effects of substitution, intercalation, non-stoichiometry and block layer concept in TiS₂ based thermoelectrics. *Phys. Chem. Chem. Phys.* **17**, 24541 (2015).
- S. Prabakar, C.W. Bumby, and R.D. Tilley: Liquid-phase synthesis of flower-like and flake-like titanium disulfide nanostructures. *Chem. Mater.* **21**, 1725 (2009).
- R.J. Toh, Z. Sofer, and M. Pumera: Catalytic properties of group 4 transition metal dichalcogenides (MX₂; M = Ti, Zr, Hf; X = S, Se, Te). *J. Mater. Chem. A* **4**, 18322 (2016).
- A.J. Huckaba, S. Gharibzadeh, M. Ralaivisoa, C. Roldan-Carmona, N. Mohammadian, G. Grancini, Y. Lee, P. Amsalem, E.J. Plichta, N. Koch, A. Moshaii, and M.K. Nazeeruddin: Low cost TiS₂ as hole transport material for perovskite solar cells. *Small Methods*, doi: 10.1002/smt.201700250. (2017).
- K.H. Park, J. Choi, H.J. Kim, D-H. Oh, J.R. Ahn, and S.U. Son: Unstable single-layered colloidal TiS₂ nanodisks. *Small* **4**, 945 (2008).
- A.R. Kirmani, G.H. Carey, M. Abdelsamie, B. Yan, D. Cha, L.R. Rollny, X. Cui, E.H. Sargent, and A. Amassian: Effect of

- solvent environment on colloidal-quantum-dot solar-cell manufacturability and performance. *Adv. Mater.* **26**, 4717 (2014).
41. A.L. Let, D.E. Mainwaring, C.J. Rix, and P. Murugaraj: Thio sol-gel synthesis of titanium disulfide thin films and nanoparticles using titanium(IV) alkoxide precursors. *J. Phys. Chem. Solids* **68**, 1428 (2007).
 42. Q. Cui, M. Sakhdari, B. Chamlagain, H-J. Chuang, Y. Liu, M.M-C. Cheng, Z. Zhou, and P-Y. Chen: Ultrathin and atomically flat transition-metal oxide: Promising building blocks for metal-insulator electronics. *ACS Appl. Mater. Interfaces* **8**, 34552 (2016).
 43. S. Jeong, D. Yoo, M. Ahn, P. Miró, T. Heine, and J. Cheon: Tandem intercalation strategy for single-layer nanosheets as an effective alternative to conventional exfoliation processes. *Nat. Commun.* **6**, 5763 (2015).
 44. L. Chen, K. Rahme, J.D. Holmes, M.A. Morris, and N.K.H. Slater: Non-solvolytic synthesis of aqueous soluble TiO₂ nanoparticles and real-time dynamic measurements of the nanoparticle formation. *Nanoscale Res. Lett.* **7**, 297 (2012).
 45. R.A.L. Morasse, T. Li, Z.J. Baum, and J.E. Goldberger: Rational synthesis of dimensionally reduced TiS₂ phases. *Chem. Mater.* **26**, 4776 (2014).
 46. G.A. Muller, J.B. Cook, H-S. Kim, S.H. Tolbert, and B. Dunn: High performance pseudocapacitor based on 2D layered metal chalcogenide nanocrystals. *Nano Lett.* **15**, 1911 (2015).
 47. M. Mousavi-Kamazani, Z. Zarghami, and M. Salavati-Niasari: Facile and novel chemical synthesis, characterization, and formation mechanism of copper sulfide (Cu₂S, Cu₂S/CuS, CuS) nanostructures for increasing the efficiency of solar cells. *J. Phys. Chem. C* **120**, 2096 (2016).
 48. K. Ramasamy, M.A. Malik, J. Raftery, F. Tuna, and P. O'Brien: Selective deposition of cobalt sulfide nanostructured thin films from single-source precursors. *Chem. Mater.* **22**, 4919 (2010).
 49. A.L. Let, D. Mainwaing, C. Rix, and P. Murugaraj: Synthesis and optical properties of TiS₂ nanoclusters. *Rev. Roum. Chim.* **52**, 235 (2007).
 50. J.F. Moulder, W.F. Stickle, P.E. Sobol, and K.D. Bomben: *Handbook of X-Ray Photoelectron Spectroscopy* (Heyden and Son, Eden Prairie, Minnesota, 1995).
 51. A.F. Carley, P.R. Chalker, J.C. Riviere, and M.W. Roberts: The identification and characterisation of mixed oxidation states at oxidised titanium surfaces by analysis of X-ray photoelectron spectra. *J. Chem. Soc., Faraday Trans. 1* **83**, 351 (1987).
 52. W. Xu, S. Zhu, Y. Liang, Z. Li, Z. Cui, X. Yang, and A. Inoue: Nanoporous CuS with excellent photocatalytic property. *Sci. Rep.* **5**, srep18125 (2015).
 53. J. Gopalakrishnan, T. Murugesan, M.S. Hegde, and C.N.R. Rao: Study of transition-metal monosulphides by photoelectron spectroscopy. *J. Phys. C: Solid State Phys.* **12**, 5255 (1979).
 54. C. Battistoni, L. Gastaldi, G. Mattogno, M.G. Simeone, and S. Viticoli: Structural and magnetic properties of layer compounds: CoGaInS₄. *Solid State Commun.* **61**, 43 (1987).
 55. D. Gonbeau, C. Guimon, G. Pfister-Guillouzo, A. Levasseur, G. Meunier, and R. Dormoy: XPS study of thin films of titanium oxysulfides. *Surf. Sci. Lett.* **254**, A476 (1991).
 56. X. Zhao, J. Jiang, Z. Xue, C. Yan, and T. Mu: An ambient temperature, CO₂-assisted solution processing of amorphous cobalt sulfide in a thiol/amine based quasi-ionic liquid for oxygen evolution catalysis. *Chem. Commun.* **68**, 9418 (2017).
 57. R.D.L. Smith, M.S. Prévot, R.D. Fagan, S. Trudel, C.P. Berlinguette, M.S. Pre, R.D. Fagan, and S. Trudel: Water oxidation catalysis: Electrocatalytic response to metal stoichiometry in amorphous metal oxide films containing iron, cobalt, and nickel. *J. Am. Chem. Soc.* **135**, 11580 (2013).

Supplementary Material

To view supplementary material for this article, please visit <https://doi.org/10.1557/jmr.2017.431>.